Earth and Planetary Science Letters 528 (2019) 115830

Contents lists available at ScienceDirect

Earth and Planetary Science Letters

www.elsevier.com/locate/epsl

Elasticity of akimotoite under the mantle conditions: Implications for multiple discontinuities and seismic anisotropies at the depth of ~600–750 km in subduction zones

Shangqin Hao[a,b], Wenzhong Wang[a,b], Wangsheng Qian[a,b], Zhongqing Wu[a,b,c,*]

[a] Laboratory of Seismology and Physics of Earth's Interior, School of Earth and Space Sciences, University of Science and Technology of China, Hefei, China
[b] National Geophysical Observatory at Mengcheng, University of Science and Technology of China, Hefei, China
[c] CAS Center for Excellence in Comparative Planetology, China

ARTICLE INFO

Article history:
Received 27 April 2019
Received in revised form 22 August 2019
Accepted 9 September 2019
Available online 2 October 2019
Editor: J. Brodholt

Keywords:
akimotoite
elasticity
multiple 660-km discontinuities
seismic anisotropy

ABSTRACT

The equation of state and elastic properties of akimotoite at simultaneously high pressures and high temperatures are obtained using first-principles calculations based on the density functional theory (DFT). The calculated results agree with the available experimental data. Combining our results with the elastic data of other minerals, we estimated the V_P, V_S, and density contrasts caused by the akimotoite-related transitions. The velocity contrasts between akimotoite and bridgmanite are 4.6% and 8.3% for V_P and V_S, respectively, which are only about half of those between majorite and akimotoite. Moreover, because both the akimotoite-bridgmanite and majorite-akimotoite transitions have broad phase boundaries, these two phase transitions may not contribute to multiple discontinuities around ~660 km depth in subduction zones as detected by seismic studies. Instead, the decomposition of pyrope into bridgmanite and corundum, which would occur in cold subduction zones with a sharp phase boundary and a large impedance contrast due to the inhibition of the pyroxene-garnet transformation at relatively low temperatures, could be a more reasonable explanation for the discontinuity at ~700–750 km in subduction zones. Furthermore, the transformation from high-pressure clinopyroxene to akimotoite at the depth of ~600 km can increase the V_P, V_S, and density by 10.1%, 14.8%, and 9.9%, respectively, indicating that the phase transition may account for the local discontinuity at ~600 km in some subduction zones. In addition, the anisotropies of akimotoite are significantly higher than those of other major minerals at the base of the mantle transition zone and could be the origin of the seismic anisotropies detected in some subduction zones.

1. Introduction

Many seismic discontinuities are closely related to the mineral phase transitions in Earth's interior. It is widely accepted that the 410-km and 660-km discontinuities are caused by the olivine-wadsleyite and post-spinel phase transitions, respectively. Beyond that, seismic studies have also detected multiple discontinuities at the depth of ~600–750 km in some subduction zones (Ai et al., 2003; Chen and Ai, 2009; Deuss et al., 2006; Gao et al., 2010; Schultz and Gu, 2013; Tibi et al., 2007; Zang et al., 2006). These complex discontinuities were expectedly ascribed to the phase transitions of non-olivine system such as the majorite-akimotoite-bridgmanite transitions at relatively low temperatures. However, Wang and Wu (2018) reported that the large wave impedance contrast caused by the decomposition of pyrope could also explain the discontinuity at the depth of ~700–750 km in subduction zones, which gives rise to a question about the exact origin of the discontinuities around ~660 km. Apparently, acquiring the wave impedance contrasts caused by all these transitions is the prerequisite for solving the conundrum. On the other hand, prominent seismic anisotropies have been found at the mantle transition zone (MTZ) and the uppermost lower mantle (ULM) in some subduction zones (Foley and Long, 2011; Nowacki et al., 2015; Vavrycuk, 2006), and the seismic anisotropies in Tonga subduction zone were interpreted as the crystallographic preferred orientation of akimotoite (Shiraishi et al., 2008). Thus the elastic properties of akimotoite are crucial in ascertaining the origins of the seismic discontinuities and anisotropies at the depth of ~600–750 km in subduction zones.

---

[*] Corresponding author at: Laboratory of Seismology and Physics of Earth's Interior, School of Earth and Space Sciences, University of Science and Technology of China, Hefei, China.

E-mail address: wuzq10@ustc.edu.cn (Z. Wu).

https://doi.org/10.1016/j.epsl.2019.115830

Akimotoite ((Mg,Fe)SiO_3) is the high-pressure polymorph of pyroxene and has an ilmenite-like structure. It usually occurs in the lower MTZ and the ULM at relatively low temperatures (Hirose, 2002; Sawamoto, 1987). Under the conditions of subduction, majorite firstly transforms into akimotoite with a positive Clapeyron slope and further becomes bridgmanite with a negative slope. In cold slab, akimotoite may be related to another different series of phase transitions. Because low temperatures can kinetically inhibit the pyroxene-garnet transformation (Nishi et al., 2013; van Mierlo et al., 2013), orthopyroxene could survive to a deeper depth at cold slab. The orthopyroxene will experience a series of phase transitions: high-pressure clinopyroxene → wadsleyite (ringwoodite) + stishovite → akimotoite → bridgmanite (Sawamoto, 1987). It is also possible that the high-pressure clinopyroxene directly transforms to akimotoite at ∼21 GPa (∼600 km) at the temperature of ∼1523–1923 K (Hogrefe et al., 1994). Therefore, the velocities and density jumps caused by these akimotoite-related phase transitions under relevant pressure and temperature (PT) conditions are significant for understanding the relationship between these phase transitions and the seismic discontinuities.

The equation of state, vibrational frequencies, and thermodynamic properties of akimotoite have been widely investigated (Hofmeister and Ito, 1992; Ito and Matsui, 1977; Karki and Wentzcovitch, 2002; Reynard et al., 1996; Wang et al., 2004; Yamanaka et al., 2005). Weidner and Ito (1985) measured the elastic tensor of akimotoite at ambient conditions using Brillouin spectroscopy. Zhou et al. (2014) measured sound velocities of akimotoite up to 25.7 GPa and 1500 K with ultrasonic interferometry techniques. The elasticity of akimotoite has also been calculated by Matsui et al. (1987) using semi-empirical potentials, by Zhang et al. (2005) using classical molecular dynamic calculations, by Da Silva et al. (1999) with first-principles calculations, and by Li et al. (2009) with first-principles molecular dynamics method.

In this study, we investigated the elastic properties of $MgSiO_3$ akimotoite at simultaneously high PT with first-principles calculations and all computational details are the same as those in previous works for the elasticity of ringwoodite, bridgmanite, periclase, and stishovite (Núñez Valdez et al., 2012; Shukla et al., 2015; Wu and Wentzcovitch, 2011; Yang and Wu, 2014). These calculations provide self-consistent and high-precision elasticity and density data for the minerals under the mantle conditions without any extrapolation and are ideal for investigating the V_P, V_S, and density contrasts of the akimotoite-related phase transitions. Combining these calculated results, we scrutinized the possible transitions related to multiple discontinuities at the depth of ∼600–750 km.

2. Method

Our calculations were performed using the Quantum ESPRESSO software package based on the density functional theory (Giannozzi et al., 2009) with local density approximation (LDA). The pseudopotential of Mg was generated using the method of von Barth and Car (Karki et al., 2000), and the pseudopotentials of O and Si were generated using Troullier-Martins method (Troullier and Martins, 1991). The cutoff energy for plane wave was 70 Ry. The structures of akimotoite were optimized using the damped variable cell shape molecular dynamics approach (Wentzcovitch et al., 1993) at variable pressures with a 4×4×4 k-point mesh. The dynamical matrices for akimotoite were calculated using density functional perturbation theory (Baroni et al., 2001) with a 2×2×2 q-point mesh and were extrapolated to a denser q mesh to obtain vibrational density of states.

According to Barron and Klein (1965), the relationship between elastic constants and the Helmholtz free energy under isothermal condition can be written as

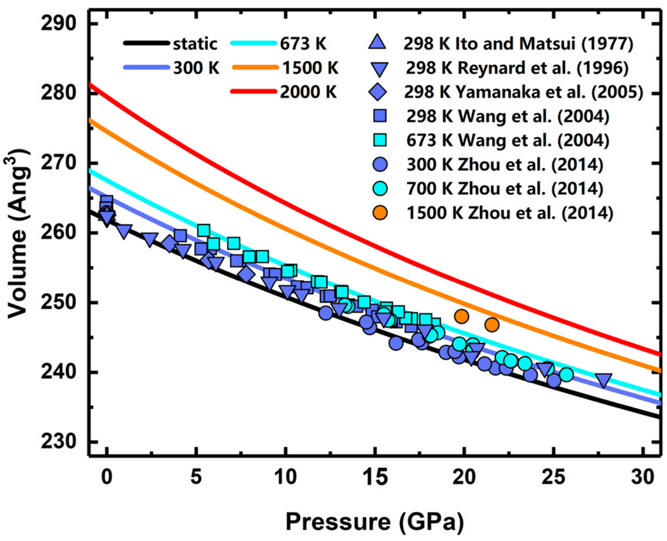

Fig. 1. Equation of states of akimotoite. The solid lines represent our calculation results, and the solid scatters are from the experimental results (Ito and Matsui, 1977; Reynard et al., 1996; Wang et al., 2004; Yamanaka et al., 2005; Zhou et al., 2014). (For interpretation of the colors in the figure(s), the reader is referred to the web version of this article.)

$$c_{ijkl}^{T}=\frac{1}{V}\left(\frac{\partial^2 F}{\partial e_{ij}\partial e_{kl}}\right)+\frac{1}{2}P(2\delta_{ij}\delta_{kl}-\delta_{il}\delta_{kj}-\delta_{ik}\delta_{jl}) \tag{1}$$

Here e_{ij} represents the infinitesimal strains and F represents the Helmholtz free energy, which can be calculated with quasi-harmonic approximation by equation (2),

$$\begin{aligned}F(V,T,e_{ij})=U_0(V,e_{ij})+\sum_{q,m}\frac{\hbar\omega_{qm}(V,e_{ij})}{2}\\+k_BT\sum_{q,m}\ln\left\{1-\exp\left[-\frac{\hbar\omega_{qm}(V,e_{ij})}{k_BT}\right]\right\}\end{aligned} \tag{2}$$

The three terms on the right side of equation (2) are the static internal, zero point, and vibrational energy, respectively. Parameters ω, q, and m represent vibrational frequency, phonon wave vector, and normal mode index, respectively. $\hbar$ and k_B are Planck and Boltzmann constants. The relationship between the Helmholtz free energies and volumes was fitted by isothermal third-order finite strain equation. The conventional method for elasticity requires vibrational density of states of many strained configurations, which need huge amount of computation. Instead, the method proposed by Wu and Wentzcovitch (2011), which only requires the vibrational density of states with an unstrained configuration, was used in this work. The method only costs a computational resource less than one-tenth of the conventional method and has been successfully applied to many minerals (Hu et al., 2016; Qian et al., 2018; Wang and Wu, 2018; Wu and Wang, 2016; Yang et al., 2017; Zou et al., 2018).

3. Results

3.1. Equation of state

The equation of states of akimotoite are shown in Fig. 1 and listed in Table 1. The calculated volumes are in good agreement with the reported experimental and calculation data (Ito and Matsui, 1977; Karki and Wentzcovitch, 2002; Li et al., 2009; Reynard et al., 1996; Wang et al., 2004; Yamanaka et al., 2005; Zhang et al., 2005; Zhou et al., 2014), especially under high PT conditions. Under the conditions of the MTZ, the volume differences between

Table 1
Equation of state parameters of akimotoite at 0 GPa.

References	T (K)	V_0 (Å^3)	K_T (GPa)	$(\partial K_T/\partial P)_T$	$(\partial K_T/\partial T)_P$ (GPa/K)
This study	static	261.83	211	4.37	
	300	265.15	202	4.40	−0.023
	1000	270.16	184	4.52	
	2000	279.51	159	4.54	
Li et al., 2009[a]	2000	275.1	158	3.7	
Karki and Wentzcovitch, 2002[a]	static	261.66	210	4.57	
Karki and Wentzcovitch, 2002[a]	300	265.20	201	4.64	−0.025
Zhang et al., 2005[b]	300	263.80	221	3.94	−0.030
Ito and Matsui, 1977	298	262.54			
Yamanaka et al., 2005	298	262.6(1)			
Reynard et al., 1996[c]	298	262.3(4)	212*	7.5(10)	
Reynard et al., 1996[d]	298	262.3(4)	212*	5.6(10)	
Wang et al., 2004[e]	298	264.2(2)	210*	4.8(5)	−0.0553(24)
Wang et al., 2004[f]	298	263.9(2)	210*	5.6(8)	−0.040(1)
Zhou et al., 2014	300	262.45(26)	207(3)	4.6*	

K_T: the isothermal bulk modulus at 0 GPa. [a] First-principles calculations; [b] Classical molecular dynamic calculations. The other data are from experimental results: [c] ruby scale; [d] ice-VII scale; [e] Au scale; [f] NaCl scale. The data marked by * represent fixed values.

our calculations and Zhou et al. (2014) are less than 0.8%. The calculated isothermal moduli K_T at ambient conditions (202 GPa) is slightly smaller than the experimental data (207–212 GPa), while the calculated $(\partial K_T/\partial P)_T$ (4.40) agrees well with most of the experimental data. In contrast, two experimental studies reported a much higher value of 5.6–7.5 for $(\partial K_T/\partial P)_T$ (Reynard et al., 1996; Wang et al., 2004). Our calculations show that the $(\partial K_T/\partial T)_P$ of akimotoite at ambient conditions is -0.023 GPa/K (Table 1) and similar to those of other minerals such as periclase, stishovite, superhydrous phase B, ringwoodite, bridgmanite, corundum and orthoenstatite (Núñez Valdez et al., 2012; Qian et al., 2018; Shukla et al., 2015; Wang and Wu, 2018; Wu and Wentzcovitch, 2011; Yang et al., 2017; Yang and Wu, 2014), all of which fall within the range from -0.02 to -0.03 GPa/K. But the experiment of Wang et al. (2004) reported smaller values of $(\partial K_T/\partial T)_P$ (-0.0553 and -0.040 GPa/K) than our result (Table 1).

3.2. *Thermal elastic properties and wave velocities*

The elastic tensor of akimotoite, totally described by seven independent elastic constants, C_{11}, C_{12}, C_{13}, C_{14}, C_{25}, C_{33}, and C_{44}, is shown in Fig. 2, and the adiabatic bulk (K_S) and shear (G) moduli, calculated using the Voigt-Reuss-Hill averages, are shown in Fig. 3a. Their derivatives with respect to PT are listed in Table S1 and Table S2. At ambient conditions, the calculated elastic moduli and their derivatives with respect to PT are in good agreement with the available experimental results (Weidner and Ito, 1985). At high pressures, the measured G of Zhou et al. (2014) is consistent with our calculations while their K_S is ~7.1–8.4% higher than our results. However, we find that the measured K_S and K_T in Zhou et al. (2014) are not self-consistent. In general, K_S can be independently derived from K_T using $K_S = K_T(1+\alpha\gamma T)$, where α and γ represent the thermal expansion and Grüneisen parameter, respectively. With the calculated thermal expansion and Grüneisen parameter, which agree well with the available experimental and calculation results (Hofmeister and Ito, 1992; Karki and Wentzcovitch, 2002), K_S is only about 1% higher than K_T at ambient conditions. In contrast, Zhou et al. (2014) show that the K_S at ambient conditions (218.9 GPa), which is determined from their experimental data of wave velocities and density, is 5.7% higher than their K_T (207 GPa) estimated from the equation of state.

All the elastic moduli significantly depend on PT. C_{14} decreases with pressure and increases with temperature, which is opposite to the PT dependences of the other elastic moduli (Fig. 2, Table S1, and Table S2). The pressure derivatives of C_{14} and C_{25} are consistent with those of Da Silva et al. (1999) and Li et al. (2009), while Matsui et al. (1987) and Zhang et al. (2005) reported reverse pressure dependences. The effect of temperature on elastic moduli decreases with pressure (Table S2). On the other hand, the pressure sensitivities of C_{11}, C_{13}, C_{33}, C_{44}, K_S, and G slightly increase with temperature (Table S1). At ambient conditions, $\partial K_S/\partial P$ and $\partial K_S/\partial T$ are 4.39 and -17.91 MPa/K, meanwhile $\partial G/\partial P$ and $\partial G/\partial T$ are 1.64 and -12.42 MPa/K. Some elastic moduli, especially C_{11}, C_{33}, C_{44}, and G, depend nonlinearly on pressure (Fig. 2 and Table S1).

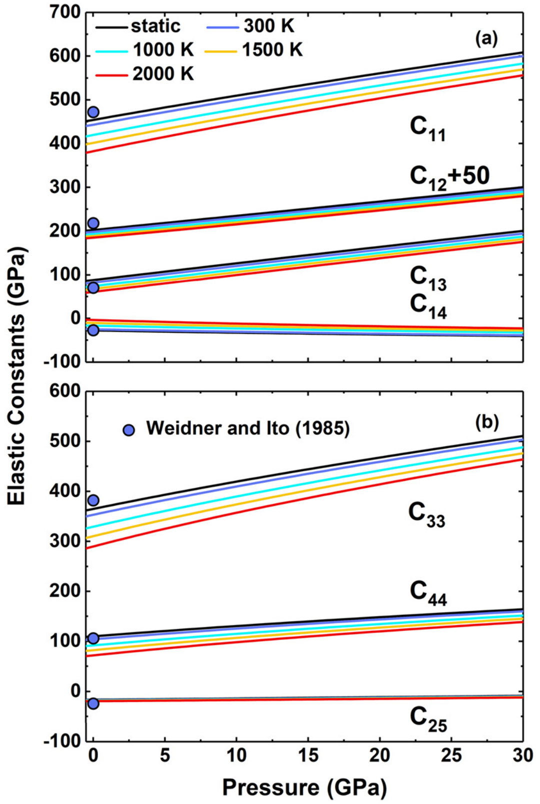

Fig. 2. Elastic constants of akimotoite at different temperatures and pressures. The solid lines are our calculation results, and the solid circles are experimental results of Weidner and Ito (1985).

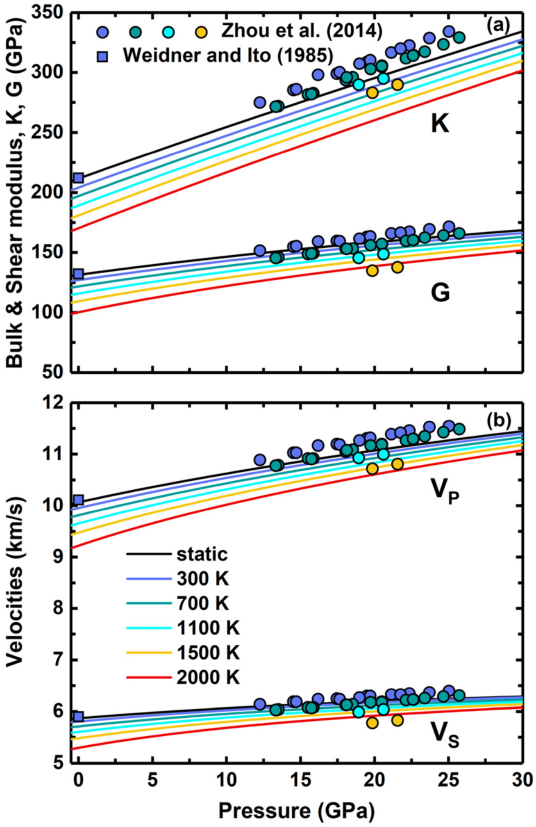

Fig. 3. (a) Bulk modulus K and shear modulus G, (b) V_P and V_S of akimotoite at various temperatures and pressures. The solid lines are our calculation results, and the solid scatters represent experimental results (Weidner and Ito, 1985; Zhou et al., 2014).

The compressional wave velocity V_P and shear wave velocity V_S, calculated from $V_P = \sqrt{(K_S + \frac{4}{3}G)/\rho}$ and $V_S = \sqrt{G/\rho}$, are shown in Fig. 3b and their PT dependences are listed in Table S3. The wave velocities at ambient conditions in Weidner and Ito (1985) are consistent with our results. The measured V_S in Zhou et al. (2014) agrees well with our data, while V_P is only consistent with our data at high temperatures but ~2.2–3.0% higher at 300 K, which agrees with the differences in K_S. On the other hand, the first derivatives of V_P and V_S in Zhou et al. (2014) are consistent with our data, while the absolute values of their second derivatives with respect to temperature are much larger than ours, exhibiting strong nonlinear behaviors of wave velocities (Table S3).

As the pressure increases, the temperature dependences of wave velocities are suppressed significantly, while their pressure dependences increase with temperature (Fig. 3b and Table S3). For instance, at 0 GPa, V_P and V_S reduced 7.4% and 8.8% from 300 K to 2000 K respectively, while the corresponding reductions at 25 GPa are 3.2% and 3.5% respectively. At ambient conditions, $\partial V_P/\partial P$ and $\partial V_S/\partial P$ are 0.062 and 0.023 km/s/GPa, meanwhile $\partial V_P/\partial T$ and $\partial V_S/\partial T$ are -3.3×10^{-4} and -2.0×10^{-4} km/s/K (Table S3). The wave velocities increase nonlinearly with pressure, which is mainly due to the nonlinear relationship between G and pressure.

3.3. Anisotropy of akimotoite

The anisotropies of akimotoite were defined as

$$A_P = 2 \times \frac{(V_P^{max} - V_P^{min})}{(V_P^{max} + V_P^{min})} \tag{3}$$

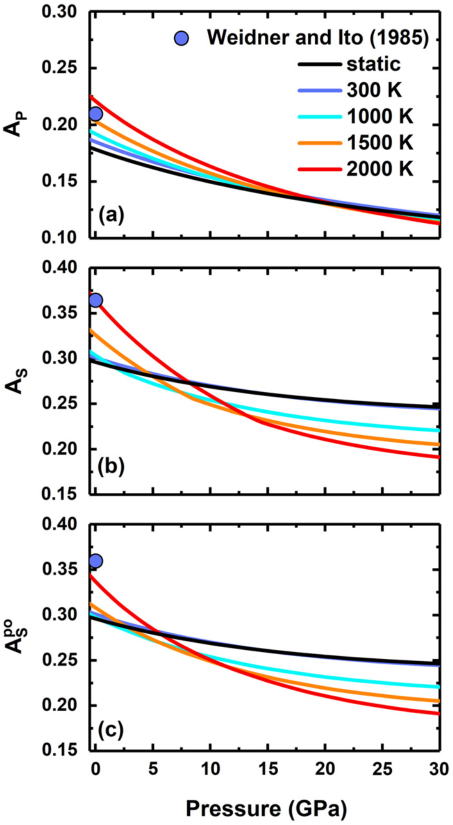

Fig. 4. (a) A_P, (b) A_S, and (c) A_S^{po} of akimotoite at different temperatures and pressures. The solid circles represent the experimental results of Weidner and Ito (1985).

$$A_S = 2 \times \frac{(V_S^{max} - V_S^{min})}{(V_S^{max} + V_S^{min})} \tag{4}$$

$$A_S^{po} = 2 \times \frac{(V_{S1} - V_{S2})_{max}}{(V_{S1} + V_{S2})} \tag{5}$$

Our calculated anisotropies of akimotoite (Fig. 4) slightly differ from the experimental results (Weidner and Ito, 1985) at ambient conditions. All of the calculated anisotropies decrease monotonously with increasing pressure at a fixed temperature, which agrees with previous calculations (Da Silva et al., 1999; Zhang et al., 2005). The anisotropies of akimotoite are significantly high under the conditions of the MTZ and ULM, with A_P of ~0.10–0.15, A_S and A_S^{po} of ~0.18–0.25.

4. Discussion

4.1. Phase transitions and multiple discontinuities at the depth of ~600–750 km in cold slabs

Multiple discontinuities at the depth of ~600–750 km have been found by seismic studies in subduction zones, especially the double discontinuities at the depth of ~660–690 km and ~700–750 km (Ai et al., 2003; Chen and Ai, 2009; Deuss et al., 2006; Gao et al., 2010; Schultz and Gu, 2013; Tibi et al., 2007; Zang et al., 2006). The double discontinuities have been interpreted as the results of the post-spinel and akimotoite-bridgmanite transitions, respectively. For a pyrolitic composition, under the conditions of cold slab, akimotoite could be stable at the bottom of the MTZ and the ULM (Fig. 5a) (Akaogi et al., 2002; Hirose, 2002; Ita and Stixrude, 1992; Vacher et al., 1998). As shown in Fig. 5a, majorite first transforms to akimotoite at the depth of ~600–660 km along the cold geotherm and further to bridgmanite at a deeper depth. Combining previous data with our results,

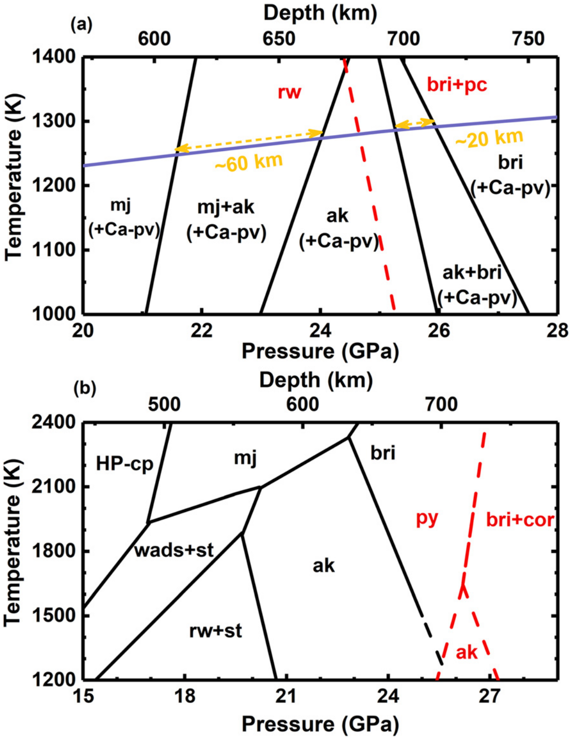

Fig. 5. (a) Phase diagrams of non-olivine system (black lines) for the pyrolitic composition (Ita and Stixrude, 1992). The post-spinel transition (red dashed line) and the cold geotherm (blue solid line, 600 K lower than normal geotherm) are also shown in this figure. The yellow dashed arrows represent the thicknesses of the majorite-akimotoite and the akimotoite-bridgmanite transitions along the geotherm. (b) Phase diagrams of $MgSiO_3$ (black lines, Sawamoto (1987)) and $Mg_3Al_2Si_3O_{12}$ (red dashed line, Kubo and Akaogi (2000)). Mineral abbreviations: mj, majorite; ak, akimotoite; bri, bridgmanite; pc, periclase; rw, ringwoodite; Ca-pv, Ca-perovskite; HP-cp, high-pressure clinopyroxene; wads, wadsleyite; st, stishovite; py, pyrope; cor, corundum.

Table 2
V_P, V_S, and density contrasts along the cold geotherm caused by major phase transitions at the depth of ~600–750 km.

Reactants	Products	dV_P (%)	dV_S (%)	$d\rho$ (%)
rw	bri + pc	4.6	10.4	8.9
mj	ak	9.5	15.7	2.6
ak	bri	4.6	8.3	6.6
rw + st	ak	−1.9	−2.6	1.2
HP-cp	ak	10.1	14.8	9.9
py	bri + cor	12.4	20.0	9.8

Data sources: akimotoite (ak) (this study), ringwoodite (rw) (Núñez Valdez et al., 2012), bridgmanite (bri) (Shukla et al., 2015), periclase (pc) (Wu and Wentzcovitch, 2011), majorite (mj) (Irifune et al., 2008), stishovite (st) (Yang and Wu, 2014), high-pressure clinopyroxene (HP-cp), pyrope (py) (Hu et al., 2016), corundum (cor) (Wang and Wu, 2018). All of the above minerals are iron-free.

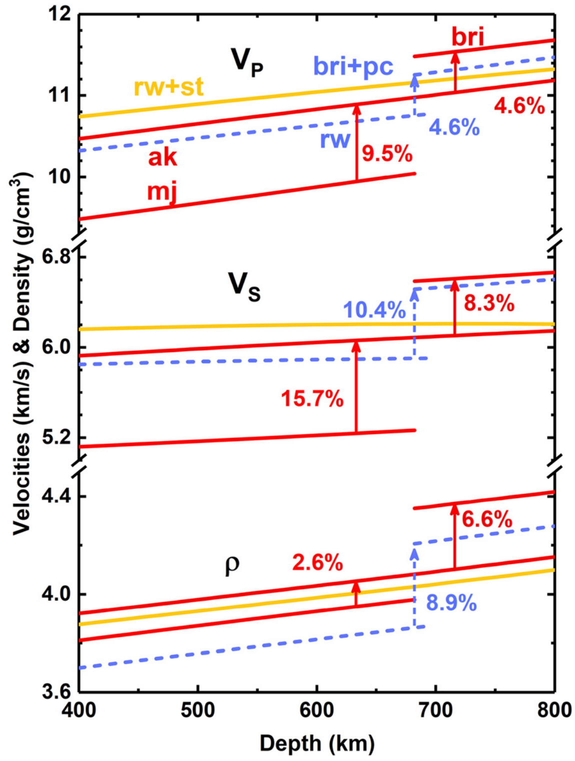

Fig. 6. V_P, V_S, and density contrasts caused by the majorite-akimotoite-bridgmanite (red solid lines and arrows) and post-spinel transitions (blue dashed lines and arrows) along the cold geotherm. The velocities and density of ringwoodite + stishovite are also shown for comparison. The data are all from the calculation results mentioned in Table 2.

we calculated the V_P, V_S, and density contrasts caused by these phase transitions at the depth of ~600–750 km along the cold geotherm (500 K lower than the normal geotherm) (Table 2 and Fig. 6). The V_P, V_S, and density contrasts between majorite and akimotoite are 9.5%, 15.7%, and 2.6%, respectively. The V_P and V_S contrasts caused by the akimotoite-bridgmanite phase transition are 4.6% and 8.3%, respectively, which are much smaller than those caused by the majorite-akimotoite phase transition. The pyrolitic mantle contains akimotoite less than ~40% (Akaogi et al., 2002; Vacher et al., 1998), thus the akimotoite-bridgmanite phase transition can cause V_P and V_S contrasts less than 1.8% and 3.3%, respectively, for the pyrolitic model. The velocity contrasts of the 738-km discontinuity in Tonga slab are about 2.2% for V_P and 2.4% for V_S (Zang et al., 2006). 2.2% jump in V_P requires the volume fraction of akimotoite of ~50%, which is obviously larger than the maximum value for the pyrolitic model, ~40%.

Whether a phase transition can result in a seismic discontinuity or not also significantly depends on its thickness. For the Al-free akimotoite ($MgSiO_3$), the akimotoite-bridgmanite transition has a sharp phase boundary with a negative Clapeyron slope, but this phase transition occurs at the depth of ~670 km (~24 GPa) even at a relatively low temperature of 1273 K (Akaogi et al., 2002), which cannot account for the discontinuity below 700 km. The presence of Al can significantly increase the transition pressure (Akaogi et al., 2002). For a pyrolitic composition, the Al-bearing akimotoite-bridgmanite transition likely occurs at the depth range of ~700–750 km at temperatures below 1200 K (Fig. 5a). However, the Al-bearing akimotoite-bridgmanite transition has a broad phase boundary larger than ~20 km (Fig. 5a) (Akaogi et al., 2002; Ita and Stixrude, 1992; Vacher et al., 1998). The akimotoite-bridgmanite transition likely results in high velocity gradients rather than a discontinuity at the depth of ~700–750 km. The majorite-akimotoite transition for a pyrolitic composition, which occurs at the depth of ~600–660 km with a phase boundary as wide as ~60 km (Fig. 5a), is also unlikely to produce a discontinuity.

Instead, the decomposition of pyrope into corundum and bridgmanite provides a more reasonable explanation for the discontinuity at the depth of ~700–750 km in subduction zone. Recent studies found that low temperatures below ~1823 K (Nishi et al., 2013) or ~1673 K (van Mierlo et al., 2013) can kinetically inhibit the pyroxene-garnet transformation. Consequently, pyrope and pyroxene in the slab may survive to the MTZ. Pyrope decomposes to bridgmanite + corundum at ~27 GPa (~739 km) above ~1500 K with a positive Clapeyron slope and a sharp phase boundary (Fig. 5b) (Kubo and Akaogi, 2000; Wang and Wu, 2018). Below ~1500 K, pyrope first transforms to akimotoite and then de-

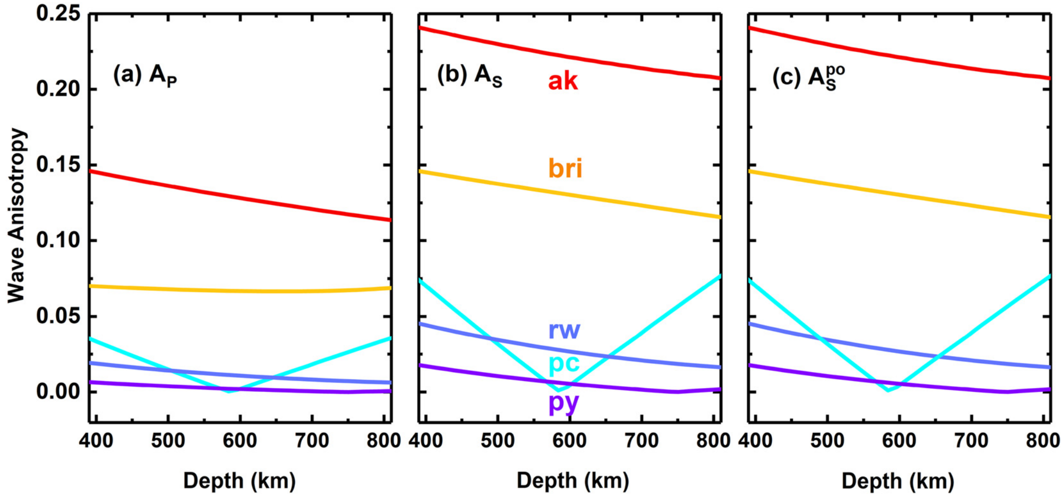

Fig. 7. (a) A_P, (b) A_S, and (c) A_S^{po} of akimotoite and other major minerals at the lower MTZ and the ULM along the cold geotherm. The data are all from the calculation results mentioned in Table 2.

composes to bridgmanite + corundum, but the two boundaries are very close and less than 1 GPa above ~1300 K (Fig. 5b). The transition of pyrope to bridgmanite + corundum can increase V_P, V_S, and density by 12.4%, 20%, and 9.8%, respectively (Wang and Wu, 2018). Therefore, the decomposition of a small amount of pyrope could result in a seismically visible discontinuity at the depth of ~700–750 km.

The surviving orthopyroxene will experience a series of phase transitions: high-pressure clinopyroxene → wadsleyite (ringwoodite) + stishovite → akimotoite → bridgmanite (Fig. 5b) (Sawamoto, 1987). Our calculations show that the V_P, V_S, and density jumps caused by the transition from ringwoodite + stishovite to akimotoite are −1.9%, −2.6%, and 1.2% respectively (Table 2 and Fig. 6), which are too weak to generate a discontinuity. Nevertheless, Hogrefe et al. (1994) found that high-pressure clinopyroxene could directly transform to akimotoite at ~21 GPa and ~1523–1923 K. The V_P, V_S, and density contrasts between high-pressure clinopyroxene and akimotoite along the cold geotherm are 10.1%, 14.8%, and 9.9% (Table 2), which likely result in a reflector or discontinuity at the depth of ~600 km in subduction zones. Therefore, there might exist three discontinuities at the depth range of ~600–750 km in subduction zone, and such three discontinuities have been observed in Northeast China, Tonga, and Nazca-South America subduction zones (Ai et al., 2003; Chen and Ai, 2009; Schultz and Gu, 2013; Zang et al., 2006), suggesting that these subduction slabs are cold enough to kinetically inhibit the pyroxene-garnet transformation.

4.2. Anisotropy of akimotoite and its implications on seismic anisotropy in subduction zones

There are noticeable seismic anisotropies at the lower MTZ and the ULM in Tonga and Nazca-South America subduction zones (Foley and Long, 2011; Nowacki et al., 2015; Vavryčuk, 2006), where the three discontinuities at the depth range of ~600–750 km were detected (Schultz and Gu, 2013; Zang et al., 2006). Both ringwoodite and pyrope should have little to do with the seismic anisotropies because of their small single-crystal elastic anisotropies (Fig. 7). Instead, akimotoite coexisting with pyrope and ringwoodite may be the major origin of the seismic anisotropies at the lower MTZ and the ULM in these subduction zones. As shown in Fig. 7, the anisotropies of akimotoite are significantly higher than those of other major minerals at the base of the MTZ. Since akimotoite is stable at low temperatures, it is very likely to exist under the PT conditions of Tonga and Nazca-South America subduction zones, especially Tonga slab, which is one of the coldest slabs. Beyond that, akimotoite will develop different crystallographic preferred orientations under plastic deformation at varying temperatures (Shiraishi et al., 2008). The temperature-dependent patterns could explain the spatially dependent seismic anisotropies of Tonga slab (Vavryčuk, 2006). Moreover, the three discontinuities detected at the depth of ~600–750 km in these slabs could provide further proof of the existence of akimotoite. All these studies suggest that the crystallographic preferred orientation of akimotoite stands a good chance of being the primary origin of the seismic anisotropies in these subduction zones.

5. Conclusion

Based on first-principles calculations within LDA, we obtained the equation of state and elastic properties of akimotoite under the mantle conditions, which agree well with previous data. Our results show that C_{14} decreases with pressure and increases with temperature, which is opposite to the PT dependences of the other elastic moduli. The effects of temperature on elastic moduli and wave velocities decrease with increasing pressure. C_{11}, C_{33}, C_{44}, and G depend nonlinearly on pressure, resulting in the nonlinear dependences of wave velocities on pressure.

Combining our results with the elastic data of other minerals, which were calculated using the same method and computational details and are ideal for investigating elasticity contrasts between minerals, we calculated the V_P, V_S, and density contrasts caused by series of phase transitions at the depth of ~600–750 km at different temperatures. The majorite-akimotoite transition increases the V_P, V_S, and density by 9.5%, 15.7%, and 2.6%, respectively, and the akimotoite-bridgmanite transition can lead to corresponding increases of 4.6%, 8.3%, and 6.6%, respectively. The velocity contrasts between akimotoite and bridgmanite are only about half of those between majorite and akimotoite. The Al-free akimotoite-bridgmanite transition has a sharp boundary but occurs at the depth above 700 km. The akimotoite-bridgmanite transition for the pyrolitic composition occurs below 700 km but has a broad phase boundary. Thus, the akimotoite-bridgmanite transitions hardly account for the discontinuity at the depth of ~700–750 km in subduction zones.

The experiments indicate that low temperatures below ~1823 K (Nishi et al., 2013) or ~1673 K (van Mierlo et al., 2013) could kinetically inhibit the pyroxene-garnet transformation. Thus pyrope in subduction zones may survive at a much deeper depth than usual. The decomposition of pyrope into bridgmanite and corundum could be a more reasonable explanation for the discontinuity at the depth of ~700–750 km due to its high impedance contrasts and sharp boundary. Meanwhile, the other surviving mineral, high-pressure clinopyroxene, could directly transform to akimotoite in cold subduction zone, causing the increases of 10.1%, 14.8%, and 9.9% in V_P, V_S, and density, respectively. The transformation may interpret another discontinuity at the depth of ~600 km in some subduction zones. Furthermore, the anisotropies of akimotoite are much higher than those of bridgmanite, pyrope, ringwoodite, and periclase. In addition, akimotoite will develop different crystallographic preferred orientations under plastic deformation at varying temperatures. Therefore, the existence of akimotoite and pyrope could account for both the seismic anisotropies and the three discontinuities around the base of the MTZ in Tonga and Nazca-South America subduction zones and also suggests that these subduction slabs are cold enough to kinetically inhibit the pyroxene-garnet transformation.

Acknowledgements

This study is supported by the "Strategic Priority Research Program" of the Chinese Academy of Sciences (XDB18000000) and the Natural Science Foundation of China (41721002). The calculations were conducted partly at the supercomputing center of University of Science and Technology of China. The data were generated by Quantum Espresso (www.quantum-espresso.org) and are available from author on request.

Appendix A. Supplementary material

Supplementary material related to this article can be found online at https://doi.org/10.1016/j.epsl.2019.115830.

References

Ai, Y.S., Zheng, T.Y., Xu, W.W., He, Y.M., Dong, D., 2003. A complex 660 km discontinuity beneath northeast China. Earth Planet. Sci. Lett. 212, 63–71.

Akaogi, M., Tanaka, A., Ito, E., 2002. Garnet–ilmenite–perovskite transitions in the system $Mg_4Si_4O_{12}$–$Mg_3Al_2Si_3O_{12}$ at high pressures and high temperatures: phase equilibria, calorimetry and implications for mantle structure. Phys. Earth Planet. Inter. 132, 303–324.

Baroni, S., de Gironcoli, S., Dal Corso, A., Giannozzi, P., 2001. Phonons and related crystal properties from density-functional perturbation theory. Rev. Mod. Phys. 73, 515–562.

Barron, T.H.K., Klein, M.L., 1965. Second-order elastic constants of a solid under stress. Proc. Phys. Soc. 85, 523–532.

Chen, L., Ai, Y.S., 2009. Discontinuity structure of the mantle transition zone beneath the North China Craton from receiver function migration. J. Geophys. Res., Solid Earth 114.

Da Silva, C.R.S., Karki, B.B., Stixrude, L., Wentzcovitch, R.M., 1999. Ab initio study of the elastic behavior of $MgSiO_3$ ilmenite at high pressure. Geophys. Res. Lett. 26, 943–946.

Deuss, A., Redfern, S.A., Chambers, K., Woodhouse, J.H., 2006. The nature of the 660-kilometer discontinuity in Earth's mantle from global seismic observations of PP precursors. Science 311, 198–201.

Foley, B.J., Long, M.D., 2011. Upper and mid-mantle anisotropy beneath the Tonga slab. Geophys. Res. Lett. 38.

Gao, Y.A., Suetsugu, D., Fukao, Y., Obayashi, M., Shi, Y.T., Liu, R.F., 2010. Seismic discontinuities in the mantle transition zone and at the top of the lower mantle beneath eastern China and Korea: influence of the stagnant Pacific slab. Phys. Earth Planet. Inter. 183, 288–295.

Giannozzi, P., Baroni, S., Bonini, N., Calandra, M., Car, R., Cavazzoni, C., Ceresoli, D., Chiarotti, G.L., Cococcioni, M., Dabo, I., Dal Corso, A., de Gironcoli, S., Fabris, S., Fratesi, G., Gebauer, R., Gerstmann, U., Gougoussis, C., Kokalj, A., Lazzeri, M., Martin-Samos, L., Marzari, N., Mauri, F., Mazzarello, R., Paolini, S., Pasquarello, A., Paulatto, L., Sbraccia, C., Scandolo, S., Sclauzero, G., Seitsonen, A.P., Smogunov, A., Umari, P., Wentzcovitch, R.M., 2009. QUANTUM ESPRESSO: a modular and open-source software project for quantum simulations of materials. J. Phys. Condens. Matter 21, 395502.

Hirose, K., 2002. Phase transitions in pyrolitic mantle around 670-km depth: implications for upwelling of plumes from the lower mantle. J. Geophys. Res., Solid Earth 107. ECV 3-1–ECV 3-13.

Hofmeister, A.M., Ito, E., 1992. Thermodynamic properties of $MgSiO_3$ ilmenite from vibrational spectra. Phys. Chem. Miner. 18, 423–432.

Hogrefe, A., Rubie, D.C., Sharp, T.G., Seifert, F., 1994. Metastability of enstatite in deep subducting lithosphere. Nature 372, 351–353.

Hu, Y., Wu, Z.Q., Dera, P.K., Bina, C.R., 2016. Thermodynamic and elastic properties of pyrope at high pressure and high temperature by first-principles calculations. J. Geophys. Res., Solid Earth 121, 6462–6476.

Irifune, T., Higo, Y., Inoue, T., Kono, Y., Ohfuji, H., Funakoshi, K., 2008. Sound velocities of majorite garnet and the composition of the mantle transition region. Nature 451, 814–817.

Ita, J., Stixrude, L., 1992. Petrology, elasticity, and composition of the mantle transition zone. J. Geophys. Res. 97, 6849.

Ito, E., Matsui, Y., 1977. Silicate ilmenites and the post-spinel transformations. In: High-Pressure Research. Elsevier, pp. 193–208.

Karki, B.B., Wentzcovitch, R.M., 2002. First-principles lattice dynamics and thermoelasticity of $MgSiO_3$ ilmenite at high pressure. J. Geophys. Res., Solid Earth 107. ECV 2-1–ECV 2-6.

Karki, B.B., Wentzcovitch, R.M., de Gironcoli, S., Baroni, S., 2000. High-pressure lattice dynamics and thermoelasticity of MgO. Phys. Rev. B 61, 8793–8800.

Kubo, A., Akaogi, M., 2000. Post-garnet transitions in the system $Mg_4Si_4O_{12}$–$Mg_3Al_2Si_3O_{12}$ up to 28 GPa: phase relations of garnet, ilmenite and perovskite. Phys. Earth Planet. Inter. 121, 85–102.

Li, L., Weidner, D.J., Brodholt, J., Alfe, D., Price, G.D., 2009. Ab initio molecular dynamics study of elasticity of akimotoite $MgSiO_3$ at mantle conditions. Phys. Earth Planet. Inter. 173, 115–120.

Matsui, M., Akaogi, M., Matsumoto, T., 1987. Computational model of the structural and elastic properties of the ilmenite and perovskite phases of $MgSiO_3$. Phys. Chem. Miner. 14, 101–106.

Nishi, M., Kubo, T., Ohfuji, H., Kato, T., Nishihara, Y., Irifune, T., 2013. Slow Si–Al interdiffusion in garnet and stagnation of subducting slabs. Earth Planet. Sci. Lett. 361, 44–49.

Nowacki, A., Kendall, J.M., Wookey, J., Pemberton, A., 2015. Mid-mantle anisotropy in subduction zones and deep water transport. Geochem. Geophys. Geosyst. 16, 764–784.

Núñez Valdez, M., Wu, Z.Q., Yu, Y.G., Revenaugh, J., Wentzcovitch, R.M., 2012. Thermoelastic properties of ringwoodite $(Fe_x,Mg_{1-x})_2SiO_4$: its relationship to the 520 km seismic discontinuity. Earth Planet. Sci. Lett. 351, 115–122.

Qian, W.S., Wang, W.Z., Zou, F., Wu, Z.Q., 2018. Elasticity of orthoenstatite at high pressure and temperature: implications for the origin of low V_P/V_S zones in the mantle wedge. Geophys. Res. Lett. 45, 665–673.

Reynard, B., Fiquet, G., Itie, J.P., Rubie, D.C., 1996. High-pressure X-ray diffraction study and equation of state of $MgSiO_3$ ilmenite. Am. Mineral. 81, 45–50.

Sawamoto, H., 1987. Phase diagram of $MgSiO_3$ at pressures up to 24 GPa and temperatures up to 2200 °C: phase stability and properties of tetragonal garnet. In: High-Pressure Research in Mineral Physics, vol. 39, pp. 209–219.

Schultz, R., Gu, Y.J., 2013. Multiresolution imaging of mantle reflectivity structure using SS and P'P' precursors. Geophys. J. Int. 195, 668–683.

Shiraishi, R., Ohtani, E., Kanagawa, K., Shimojuku, A., Zhao, D., 2008. Crystallographic preferred orientation of akimotoite and seismic anisotropy of Tonga slab. Nature 455, 657–660.

Shukla, G., Wu, Z.Q., Hsu, H., Floris, A., Cococcioni, M., Wentzcovitch, R.M., 2015. Thermoelasticity of Fe^{2+}-bearing bridgmanite. Geophys. Res. Lett. 42, 1741–1749.

Tibi, R., Wiens, D.A., Shiobara, H., Sugioka, H., Yuan, X., 2007. Double seismic discontinuities at the base of the mantle transition zone near the Mariana slab. Geophys. Res. Lett. 34.

Troullier, N., Martins, J.L., 1991. Efficient pseudopotentials for plane-wave calculations. Phys. Rev. B 43, 1993–2006.

Vacher, P., Mocquet, A., Sotin, C., 1998. Computation of seismic profiles from mineral physics: the importance of the non-olivine components for explaining the 660 km depth discontinuity. Phys. Earth Planet. Inter. 106, 275–298.

van Mierlo, W.L., Langenhorst, F., Frost, D.J., Rubie, D.C., 2013. Stagnation of subducting slabs in the transition zone due to slow diffusion in majoritic garnet. Nat. Geosci. 6, 400–403.

Vavrycuk, V., 2006. Spatially dependent seismic anisotropy in the Tonga subduction zone: a possible contributor to the complexity of deep earthquakes. Phys. Earth Planet. Inter. 155, 63–72.

Wang, W.Z., Wu, Z.Q., 2018. Elasticity of corundum at high pressures and temperatures: implications for pyrope decomposition and Al-content effect on elastic properties of bridgmanite. J. Geophys. Res., Solid Earth 123, 1201–1216.

Wang, Y.B., Uchida, T., Zhang, J.Z., Rivers, M.L., Sutton, S.R., 2004. Thermal equation of state of akimotoite $MgSiO_3$ and effects of the akimotoite–garnet transformation on seismic structure near the 660 km discontinuity. Phys. Earth Planet. Inter. 143, 57–80.

Weidner, D.J., Ito, E., 1985. Elasticity of $MgSiO_3$ in the ilmenite phase. Phys. Earth Planet. Inter. 40, 65–70.

Wentzcovitch, R.M., Martins, J.L., Price, G.D., 1993. Ab initio molecular dynamics with variable cell shape: application to $MgSiO_3$. Phys. Rev. Lett. 70, 3947–3950.

Wu, Z., Wang, W., 2016. First-principles calculations of elasticity of minerals at high temperature and pressure. Sci. China Earth Sci. 59, 1107–1137.

Wu, Z.Q., Wentzcovitch, R.M., 2011. Quasiharmonic thermal elasticity of crystals: an analytical approach. Phys. Rev. B 83, 184115.

Yamanaka, T., Komatsu, Y., Sugahara, M., Nagai, T., 2005. Structure change of $MgSiO_3$, $MgGeO_3$, and $MgTiO_3$ ilmenites under compression. Am. Mineral. 90, 1301–1307.

Yang, D.P., Wang, W.Z., Wu, Z.Q., 2017. Elasticity of superhydrous phase B at the mantle temperatures and pressures: implications for 800 km discontinuity and water flow into the lower mantle. J. Geophys. Res., Solid Earth 122, 5026–5037.

Yang, R., Wu, Z.Q., 2014. Elastic properties of stishovite and the $CaCl_2$-type silica at the mantle temperature and pressure: an ab initio investigation. Earth Planet. Sci. Lett. 404, 14–21.

Zang, S.X., Zhou, Y.Z., Ning, J.Y., Wei, R.Q., 2006. Multiple discontinuities near 660 km beneath Tonga area. Geophys. Res. Lett. 33.

Zhang, Y.G., Zhao, D.P., Matsui, M., 2005. Anisotropy of akimotoite: a molecular dynamics study. Phys. Earth Planet. Inter. 151, 309–319.

Zhou, C.Y., Greaux, S., Nishiyama, N., Irifune, T., Higo, Y., 2014. Sound velocities measurement on $MgSiO_3$ akimotoite at high pressures and high temperatures with simultaneous in situ X-ray diffraction and ultrasonic study. Phys. Earth Planet. Inter. 228, 97–105.

Zou, F., Wu, Z.Q., Wang, W.Z., Wentzcovitch, R.M., 2018. An extended semianalytical approach for thermoelasticity of monoclinic crystals: application to diopside. J. Geophys. Res., Solid Earth 123, 7629–7643.